Heavy-impurity resonance, hybridization, and phonon spectral functions in $Fe_{1-x}M_xSi$ (M= Ir, Os)

O. Delaire,[*] I. I. Al-Qasir, A. F. May, C. W. Li, and B. C. Sales
Materials Science and Technology Division, Oak Ridge National Laboratory, Oak Ridge, Tennessee 37831, USA

J. L. Niedziela
Instrument and Source Division, Oak Ridge National Laboratory, Oak Ridge, Tennessee 37831, USA

J. Ma, M. Matsuda, and D. L. Abernathy
Quantum Condensed Matter Division, Oak Ridge National Laboratory, Oak Ridge, Tennessee 37831, USA

T. Berlijn
Center for Nanophase Materials Sciences and Computer Science and Mathematics Division, Oak Ridge National Laboratory,
Oak Ridge, Tennessee 37831-6494, USA

(Received 8 November 2014; revised manuscript received 15 January 2015; published 31 March 2015)

The vibrational behavior of heavy substitutional impurities (M = Ir, Os) in $Fe_{1-x}M_xSi$ (x = 0,0.02,0.04,0.1) was investigated with a combination of inelastic neutron scattering (INS), transport measurements, and first-principles simulations. Our INS measurements on single crystals mapped the four-dimensional dynamical structure factor, $S(\mathbf{Q},E)$, for several compositions and temperatures. Our results show that both Ir and Os impurities lead to the formation of a weakly dispersive resonance vibrational mode, in the energy range of the acoustic phonon dispersions of the FeSi host. We also show that Ir doping, which introduces free carriers, leads to softened interatomic force constants compared to doping with Os, which is isoelectronic to Fe. We analyze the phonon $S(\mathbf{Q},E)$ from INS through a Green's-function model incorporating the phonon self-energy based on first-principles density functional theory simulations, and we study the disorder-induced lifetimes on large supercells. Calculations of the quasiparticle spectral functions in the doped system reveal the hybridization between the resonance and the acoustic phonon modes. Our results demonstrate a strong interaction of the host acoustic dispersions with the resonance mode, likely leading to the large observed suppression in lattice thermal conductivity.

DOI: 10.1103/PhysRevB.91.094307 PACS number(s): 63.20.−e, 63.20.Ry, 78.70.Nx, 84.60.Rb

I. INTRODUCTION

Understanding microscopic phonon-scattering mechanisms is important for the rational design of materials for specific energy technologies. For thermoelectric applications, it is important to suppress the thermal conductivity by scattering phonons in order to maximize the thermoelectric efficiency [1]. Mass-mismatch scattering of phonons in thermoelectric alloys is a broadly adopted strategy to hinder phonon propagation, for example in Si-Ge alloys [2,3], half-Heusler compounds [4–7], skutterudites [8–10], and other compounds. Isotopic-impurity scattering, where the mass contrast is relatively low and the force constants unperturbed, has been theoretically investigated using perturbation theory [11,12], resulting in formulas that are widely used. However, in the case of large mass contrast, some of the approximations used in these derivations become questionable. Thus, it is particularly interesting to investigate the effect of heavy impurities, which are efficient at disrupting phonon propagation, on the scattering rates and velocities of acoustic phonons. To this end, phonons in $Fe_{1-x}M_xSi$ (M = Ir, Os) were investigated with a combination of inelastic neutron-scattering measurements, transport measurements, and first-principles simulations.

Despite its simple chemical formula, FeSi is an unusual material and has attracted longstanding interest. At low pressure and low temperature, FeSi crystallizes in the B20 cubic structure [13]. It transforms to the simpler B2 phase (CsCl type) under high pressure and high temperature [14]. The B20 structure can be viewed as a strongly distorted rocksalt structure, with Fe-Si nearest-neighbor pairs distorted along $\langle 111 \rangle$ directions, resulting in sevenfold coordination at the Fe and Si sites, and low symmetry (T^4 $P2_13$), [13]. Many properties of FeSi show anomalous temperature dependences. For example, the magnetic susceptibility, heat capacity, thermal expansion, and elastic properties all show anomalous temperature dependences between 0 and 800 K [15–17]. These have been related to the very narrow gap in the electronic band structure [15,16,18–23]. In addition, it has been shown that phonon excitations at finite temperature can close the narrow gap, accounting for some of the observed anomalous temperature dependences [24–30], in particular the experimental observation of the gap closing [31–33]. Possibly strong electronic correlations have also been noted [34,35], and it has been proposed that FeSi could be an unusual d-electron Kondo insulator, although this point remains controversial [32,34,36–39]. Interest in FeSi also arises from geophysics, as it is a possible reaction product between molten iron and mantle silicates at the core-mantle boundary [14,40–42].

We have reported in a previous study that the phonon density of states (DOS) of FeSi softens dramatically more than

---

[*] delaireoa@ornl.gov

is expected from the quasiharmonic (QH) theory, while the isostructural compound CoSi (metallic at all temperatures) follows a typical QH softening [28]. This behavior was explained by the sensitivity of the electronic structure of FeSi to thermal disorder, as phonon excitations perturb the lattice sufficiently to cause the metallization of the system at $T \gtrsim 200$ K, in turn leading to strong phonon softening [24,28]. Electron-phonon coupling was also investigated in Refs. [43,44]. This thermal behavior was contrasted with high-pressure measurements, which showed that at constant temperature, the phonons behave quasiharmonically upon compression [30]. Related effects of doping and temperature on the electronic structure and phonons in transition metals were reported in [45–47].

Transport measurements in FeSi doped with Os, Ir, or Co (substituting for Fe) have also shown that the electron-phonon coupling is strong, with carriers (extra electrons from Ir or Co doping) causing a considerable suppression of the lattice thermal conductivity, κ_{lat} [29]. In addition, the heavy impurities Ir and Os induce a strong mass-defect scattering of phonons, owing to a mass perturbation $M_{\mathrm{Ir}}/M_{\mathrm{Fe}} = 3.44$ and $M_{\mathrm{Os}}/M_{\mathrm{Fe}} = 3.41$, respectively. This mass-defect scattering in the case of Os impurities, which do not introduce carriers, causes a suppression of $\kappa_{\mathrm{lat}}^{\mathrm{max}}$ by a factor of three at 70 K. In the present study, we investigate the vibrational behaviors of these heavy impurities, and their effect on the host acoustic phonons.

We performed transport measurements, inelastic neutron-scattering (INS) measurements on powders and single crystals, as well as first-principles simulations of phonons with density functional theory (DFT). Our phonon measurements and simulations identify the formation of a heavy-impurity resonance mode upon substituting a few percent of Fe atoms with either Os or Ir. Our DFT simulations reproduce the overall phonon dispersions and dynamical structure factor of the host FeSi quantitatively. In addition, supercell calculations on the phonon quasiparticle spectral functions in the doped system also predict the formation of a resonance mode, and conclusively show the hybridization of the resonance with the acoustic phonon branches.

II. SAMPLE PREPARATION

Polycrystalline ingots of FeSi, $\mathrm{Fe_{0.9}Ir_{0.1}Si}$, and $\mathrm{Fe_{0.9}Os_{0.1}Si}$ were prepared by arc melting pieces of the respective elements (better than 99.99% purity) in appropriate proportions, under an ultrapure Ar atmosphere. The ingots were melted several times to ensure homogeneity, which is particularly important given the high melting points of Os/Ir relative to Fe and Si. No oxidation was detected on the ingots after melting. The mass loss upon arc melting was negligible. The resulting ingots were pulverized and examined with x-ray diffraction. The x-ray-diffraction patterns for all samples were consistent with the B20 structure, and no secondary phase was observed.

Single crystals of FeSi, $\mathrm{Fe_{0.98}Os_{0.02}Si}$, and $\mathrm{Fe_{1-x}Ir_xSi}$ ($x = 0.02,0.04$) were prepared for transport and neutron-scattering measurements. The Os- and Ir-doped single crystals were prepared using a four-mirror, xenon lamp floating-zone furnace from Crystal Systems. The crystal growth was conducted in an argon atmosphere, after purging the system for many hours with high-purity argon passed through a Ti gettering furnace at 800 °C. Growth rates of approximately 15° mm/h were employed, and crystals approaching 3×50 mm were obtained. Smaller pieces were utilized to study the phonons in the doped systems to promote homogeneity. The crystals are identified by the nominal compositions of the polycrystalline feed rods: $\mathrm{Fe_{0.98}Os_{0.02}Si}$ and $\mathrm{Fe_{0.98}Ir_{0.02}Si}$. In addition, a large single crystal of undoped FeSi was synthesized by the Czochralski method, using 99.99% vacuum remelted iron and 99.999% semiconductor grade silicon, as detailed in [15]. A coinlike piece weighing about 8 grams was cut from the growth using an electric spark saw, for neutron-scattering measurements.

For the single-crystal synthesis in the optical furnace, polycrystalline feed and seed rods of nominal composition $\mathrm{Fe_{1-x}Ir_xSi}$ and $\mathrm{Fe_{1-x}Os_xSi}$ were prepared by first arc melting high-purity elements on a water-cooled copper hearth (15–20 g total load). The resulting material was milled in a planetary ball mill at 400 rpm for 60 min using a $\mathrm{Si_3N_4}$ vial and balls loaded and sealed inside a helium glove box. This resulted in a fine-grain powder that required handling inside a glove box to prevent oxidation. The material was then loaded inside a balloon, which was tied off inside the glove box. Balloons were pressed under hydrostatic pressures of approximately 12 000 psi for 15 min. The rods were extracted from the balloons in the glove box and transferred to quartz ampoules, which were then sealed under vacuum. The polycrystalline rods were sintered at 1050 °C for 12 h, which resulted in very dense polycrystalline rods.

III. PHYSICAL PROPERTY CHARACTERIZATION

The samples were characterized by electrical and thermal transport measurements using the Physical Property Measurement System (PPMS) from Quantum Design. These measurements were performed using the Thermal Transport Option, with gold-coated copper leads attached to the samples using silver epoxy (H20E Epo-Tek). Powder x-ray-diffraction (pXRD) data were collected at ambient conditions, using a PANalytical X'Pert Pro MPD using a Cu Kα_1 monochromator. Rietveld refinement of the data, using the published structure, demonstrated an incorporation of Ir and Os into the lattice via lattice expansion: $a = 4.4858(1)$ Å for FeSi (floating-zone growth) and $a = 4.4923(1)$ Å for both $\mathrm{Fe_{0.98}Os_{0.02}Si}$ and $\mathrm{Fe_{0.98}Ir_{0.02}Si}$, consistent with the similarly large sizes of Ir and Os. Smooth lattice expansion was observed for nominal compositions up to $\mathrm{Fe_{0.92}Os_{0.08}Si}$ and $\mathrm{Fe_{0.8}Ir_{0.2}Si}$, though the higher concentrations of Ir/Os are not utilized in this study. Thus, the compositions examined here are well within the solubility limits for Ir/Os in FeSi. However, higher concentrations of Os seemed to lead to poorer crystal growth. Indeed, compositional fluctuations were observed in these samples via energy dispersive spectroscopy.

Transport properties were measured (Fig. 1) to confirm that the floating-zone grown samples behave as expected. Indeed, the crystals grown by the floating-zone technique have qualitatively similar electrical resistivity (ρ), Seebeck coefficient (α), and thermal conductivity (κ) as polycrystalline samples with Ir and Os doping [29]. Similarly, the transport properties of the undoped FeSi are observed to be similar to the FeSi crystal grown by the Czochralski method [29].

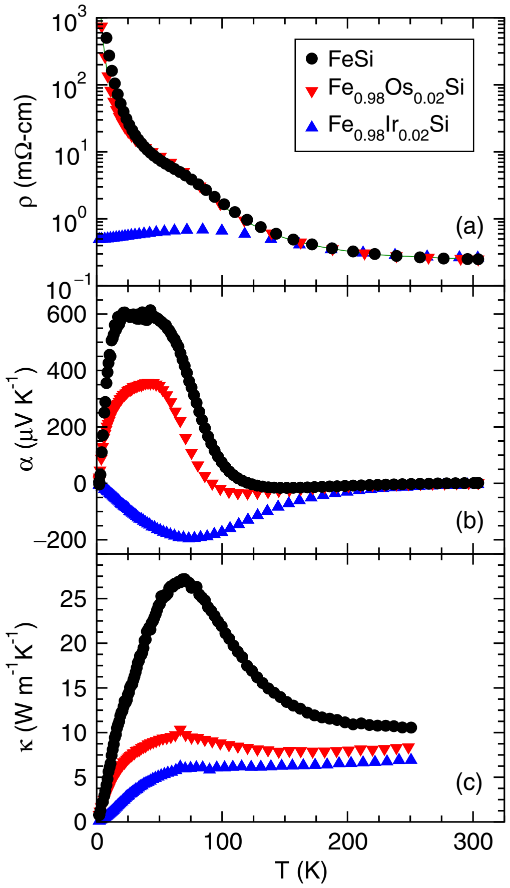

FIG. 1. (Color online) (a) Resistivity ρ, (b) Seebeck coefficient α, and (c) thermal conductivity κ for single-crystalline samples of FeSi, $Fe_{0.98}Os_{0.02}Si$, and $Fe_{0.98}Ir_{0.02}Si$ grown by the optical floating-zone technique.

We note that the electron doping (negative α and reduced ρ) induced by Ir substitution is clearly observed, which demonstrates that the dopant atom is indeed entering the lattice as expected. The electrical properties of the Os-doped sample are similar to those of the undoped FeSi sample, as expected for samples with the same nominal electron count. The unusual electronic-transport properties of FeSi have long been of interest to the condensed-matter community, and in this paper we focus on the influence that these dopants have on the lattice dynamics and thermal conductivity.

IV. INELASTIC NEUTRON SCATTERING

Inelastic neutron-scattering spectra were measured on powder samples and single crystals using the Wide Angular Range Chopper Spectrometer (ARCS) at the Spallation Neutron Source (SNS) at Oak Ridge National Laboratory (ORNL) [48]. The different powder samples (each about 10 g) were loaded into identical thin-walled Al containers, and placed in an evacuated closed-cycle refrigerator. Measurements were performed using incident neutron energies $E_i = 80$ and 40 meV. For $E_i = 80$ meV, the energy resolution is about 1.5 meV at 60 meV neutron energy loss, increasing to 3.2 meV at the elastic line. The elastic peak was subtracted and the low-energy part of phonon DOS was extrapolated with a Debye-like parabolic energy dependence for $E < 7$ meV. The data were normalized by the total incident flux, corrected for detector efficiency, and mapped from instrument coordinates to the physical momentum transfer Q and energy transfer E using the MANTID reduction software [49]. The scattering from the empty Al container was measured and analyzed in the same conditions as the samples, and subtracted from the data for each composition. The analysis of the phonon DOS was performed in the incoherent scattering approximation, which is reliable in the case of powders and large integration volumes in reciprocal space.

For a monatomic crystal of cubic symmetry, this analysis provides the phonon DOS. However, in a polyatomic crystal, elements have different ratios of cross section over mass, σ/M, and the vibration modes corresponding to motions of elements with larger σ/M are overemphasized, resulting in a generalized phonon DOS [50]. The values of σ/M for Fe, Ir, Os, Si are 0.208, 0.077, 0.073 0.077 b/amu, respectively. Thus, the modes involving large motions of Fe atoms are overemphasized in the measured phonon DOS. However, when x is small, the change in neutron weights between FeSi and $Fe_{1-x}Os_xSi$ or $Fe_{1-x}Ir_xSi$ are not a concern, enabling a straightforward comparison for alloying effects.

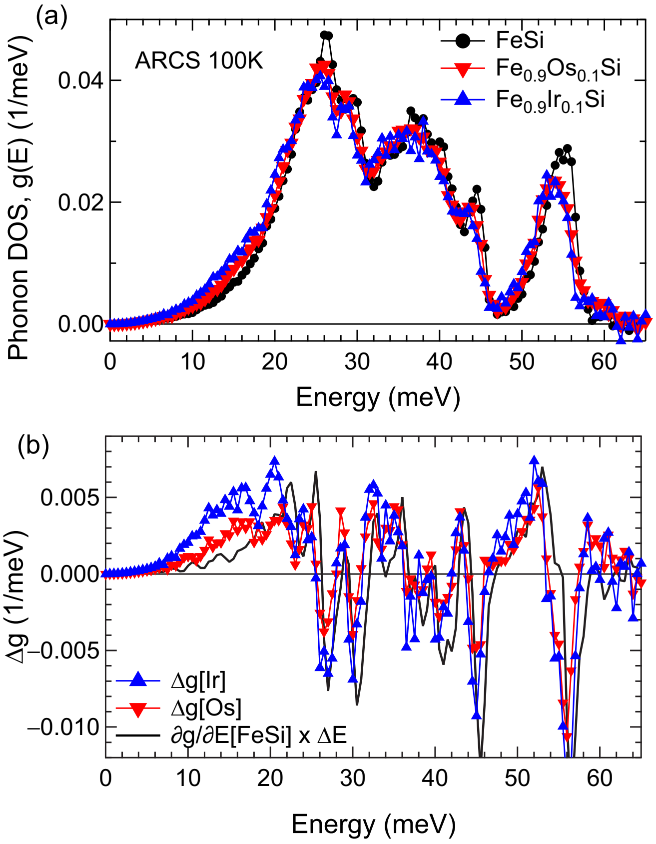

FIG. 2. (Color online) (a) Phonon DOS of FeSi, $Fe_{0.9}Os_{0.1}Si$, and $Fe_{0.9}Ir_{0.1}Si$, measured with INS at $T = 100$ K ($E_i = 80$ meV). Statistical error bars are comparable to the size of the symbols. (b) Difference in phonon DOS between the doped samples and pure FeSi, normalized to one impurity atom, compared with the energy derivative of FeSi DOS.

Figure 2(a) shows the phonon DOS measured on powder samples at $T = 100$ K. As can be seen, substituting 10% of Fe atoms with Os or Ir leads to an overall softening of the phonon spectrum. The average energies for FeSi, $\mathrm{Fe_{0.9}Os_{0.1}Si}$, and $\mathrm{Fe_{0.9}Ir_{0.1}Si}$ are 33.8 ± 0.1, 33.1 ± 0.1, and 31.6 ± 0.1 meV, respectively. In Fig. 2(b), we show the difference in the DOS between the doped and undoped materials, compared with the energy derivative of the FeSi DOS. The good agreement in the features above 20 meV indicates that the change in the spectrum is mainly a shift to lower energy. However, between 10 and 20 meV, an additional component is evident besides the shift, with an excess of spectral weight centered around 15 meV, which is most pronounced for the Ir-doped sample. Such enhancements have previously been observed for heavy impurities forming resonance modes, corresponding to local dynamics decoupled from that of the lattice [51,52]. We show in detail below that both Os and Ir dopants lead to the formation of resonance modes for all of the concentrations we investigated. The larger excess for Ir than for Os impurities can be attributed to the softer force constants around Ir atoms, which are screened by an extra *d* electron, making the system metallic (also reflected in the resistivity data of Fig. 1). This result is confirmed from our first-principles calculations, as discussed below.

The overall softening of the phonon DOS results from a combination of several factors. Both Os and Ir ions are larger than the Fe ion. The FeSi and $\mathrm{Fe_{0.9}Ir_{0.1}Si}$ experimental lattice parameters are 4.486 Å and 4.51 Å, respectively, at 295 K [15]. The lattice parameter of FeSi at 5 K is 4.475 Å [15]. Assuming the lattice parameters ratio at 100 K is the same ratio (1.00535) at 300 K between $\mathrm{Fe_{0.9}Os_{0.1}Si}$ and FeSi, we expect the lattice parameter of $\mathrm{Fe_{0.9}Os_{0.1}Si}$ at 5 K is 4.499 Å. On the other hand, it is expected that the lattice parameter of $\mathrm{Fe_{0.9}Os_{0.1}Si}$ is very close to that of $\mathrm{Fe_{0.9}Ir_{0.1}Si}$, that is, both systems have a volume increase of the unit cell of about 1.6% with respect to the FeSi volume unit cell. This increase in volume can explain the decrease in energy by 2% in the case of $\mathrm{Fe_{0.9}Os_{0.1}Si}$ (using a Grüneisen parameter $\gamma = 1.6$), but is not enough to explain the softening of 6.3% in the case of $\mathrm{Fe_{0.9}Ir_{0.1}Si}$. Mass effects also have to be considered. The doping with 10% of Os or Ir leads to an average mass increase of 16.0% and 16.3% per formula unit, respectively. Since Os and Ir dopings lead to nearly the same mass increase, this cannot explain the difference in phonon frequency between the two doped systems. Thus, the larger softening in the case of Ir dopants arises from the weaker interatomic force constants associated with the augmented screening from the free carriers. This change in local force constants was corroborated with first-principles calculations, as detailed below.

In order to investigate the resonance modes in more detail, momentum-resolved measurements were performed on single crystals of FeSi (mass = 8.64 g), $\mathrm{Fe_{0.98}Os_{0.02}Si}$ (mass = 2.06 g), and $\mathrm{Fe_{0.96}Ir_{0.04}Si}$ (two coaligned crystals; total mass = 5.5 g). Using the ARCS time-of-flight spectrometer at the Spallation Neutron Source, large swaths of the four-dimensional dynamical structure factor, $S(\mathbf{Q},E)$, were mapped at several temperatures. The single-crystal measurements on ARCS were performed with an incident neutron energy $E_i = 40$ meV, and with the (H,H,L) crystallographic plane of the samples mounted in the horizontal plane. Additional measurements were performed with the HB-1 triple-axis spectrometer at the High Flux Isotope Reactor (HFIR). In the triple-axis measurements, the monochromator and analyzer were pyrolytic graphite (PG002). We used an instrument collimation of $48' - 40' - 40' - 120'$ in all measurements (vertical collimation only). The samples were aligned in the (H,H,L) scattering plane and mounted inside a helium-filled can, cooled with a closed-cycle helium refrigerator. Spectra were measured in constant-Q mode at the center of the (113) Brillouin zone on $\mathrm{Fe_{0.98}Os_{0.02}Si}$ and $\mathrm{Fe_{0.98}Ir_{0.02}Si}$ at $T = 50$ and 300 K, and on $\mathrm{Fe_{0.96}Ir_{0.04}Si}$ at $T = 100$ and 300 K. Measurements were performed with constant $E_f = 14.7$ meV (and additional measurements with $E_f = 13.5$ meV).

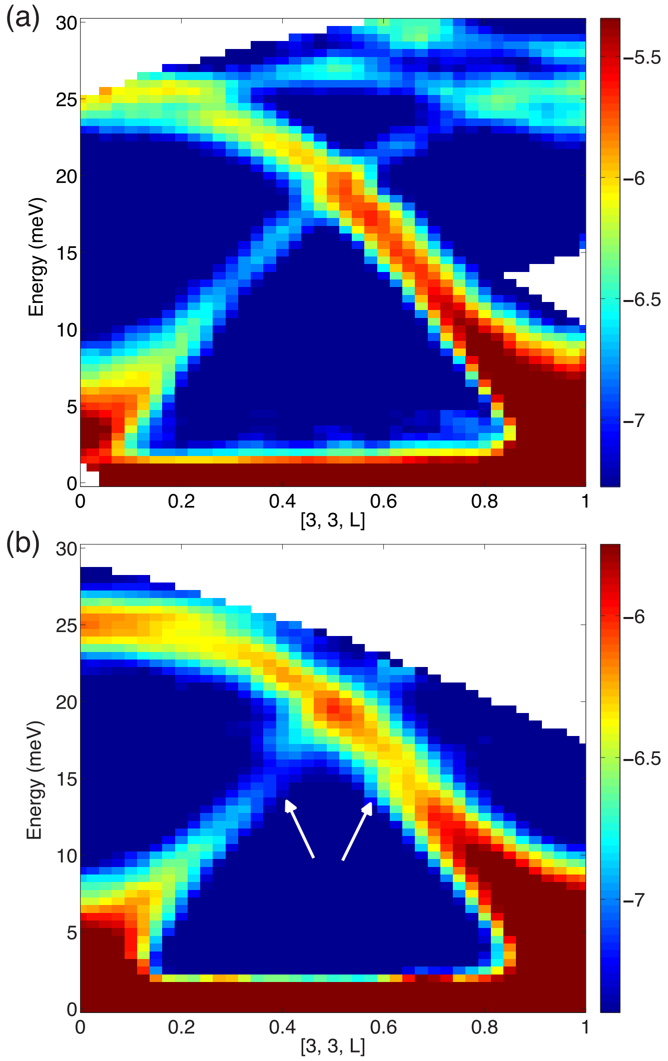

FIG. 3. (Color online) Single-crystal scattering function $S(\mathbf{Q},E)$ for (a) FeSi and (b) $\mathrm{Fe_{0.96}Ir_{0.04}Si}$, along the Γ-X direction $[3,3,L]$, measured with ARCS at $T = 100$ K. The TA branch shows a clear splitting at $L = 0.37, 0.63$ in the doped sample, as indicated by the white arrows. The white areas correspond to missing data.

Figure 3 shows slices of $S(\mathbf{Q},E)$ in the Γ-X direction at 100 and 300 K for FeSi and $\mathrm{Fe_{0.96}Ir_{0.04}Si}$ in the Brillouin zone (3, 3, 1) from ARCS measurements. As may be seen here, in the case of $\mathrm{Fe_{0.96}Ir_{0.04}Si}$, the transverse acoustic (TA) dispersion branch (doubly degenerate) shows a clear anomaly

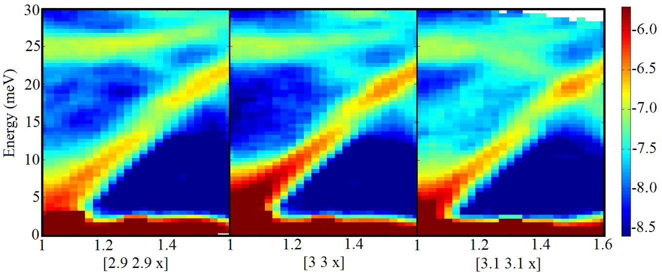

FIG. 4. (Color online) Single-crystal scattering function $S(\mathbf{Q},E)$ for $Fe_{0.96}Ir_{0.04}Si$ along $[3,3,L]$ and slightly off the high-symmetry direction at $[2.9,2.9,L]$ and $[3.1,3.1,L]$, measured with ARCS at 100 K. The kink in the TA dispersions is seen around 17 meV in the three panels ($L \sim 1.37$).

around $q = [0,0,0.36]$, compared to the undoped FeSi crystal. A kink in the dispersion as well as a local minimum in the scattering intensity simultaneously occur at this wave vector. In addition, the kink is observed at the same wave vector for both temperatures measured, and was also observed at equivalent wave vectors in other Brillouin zones. The same behavior is also clearly observed for wave vectors slightly off the [001] high-symmetry direction, for example, along $(2.9,2.9,L)$ and $(3.1,3.1,L)$, as shown in Fig. 4.

This feature is characteristic of the interaction between the acoustic phonon dispersions of the host lattice and the resonance mode associated with the heavy impurities [51]. The energy of the kink is about 17 meV, which matches well with the energy of the resonance mode observed in HB-1 measurements (Fig. 5), and also matches the Q-integrated excess intensity in the phonon DOS [Figs. 2(a) and 2(b)] and our first-principles simulations (see below).

As can be seen in Fig. 5, a peak is observed in the HB-1 spectra acquired at the (113) zone center, at $E \simeq 17$ meV for both dopants, for both temperatures. Since the lowest-energy optical modes at Γ have energies in excess of 23 meV, this peak can be associated with the resonance mode of Os and Ir impurity atoms, which is confirmed below using first-principles simulations. We note that triple-axis measurements can be affected by background effects and spurious peaks [53], and for this reason we have also measured the empty Al holder and can inside the Displex (300 K only), in the same conditions as the samples (same instrument collimation and same opening of boron-nitride masking slits, positioned just before and just after the sample environment). The background contribution is shown as green circles in Figs. 5(a) and 5(b). The background shows a broad bump of intensity centered at about 20 meV (a Gaussian fit finds 19.6 meV), roughly at the position of the local minimum of intensity for doped FeSi (between the resonance and lowest-energy optical mode at Γ), and about 2 meV higher than the resonance peak. The bump in the background is also considerably broader than the signal at 17 meV. We also reemphasize that the resonance at 17 meV is seen as an enhancement of the DOS of doped samples at that energy [Fig. 2(a)], and that the empty-can background was subtracted from the data for powder samples. Also, compared with the effects described in [53], our samples are strong scatterers, and only a minimal amount of aluminum was used to hold them in the neutron beam.

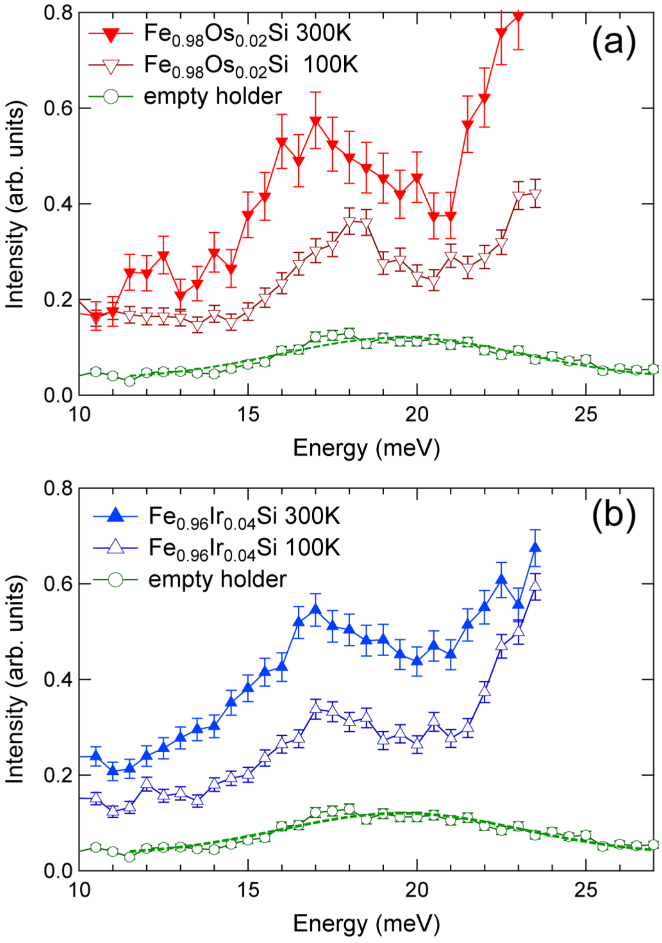

FIG. 5. (Color online) Neutron-scattering spectra for single crystals of (a) $Fe_{0.98}Os_{0.02}Si$ and (b) $Fe_{0.96}Ir_{0.04}Si$, measured with the HB1 triple-axis spectrometer, at 100 and 300 K. The spectra were measured at the center of the (1,1,3) Brillouin zone (Γ point). The green circles show the background from the same Al holder and can be used to mount the samples, measured at 300 K (same collimation and aperture slits). The dashed green curve is a Gaussian fit to the background (centered at 19.6 meV).

V. FIRST-PRINCIPLES SIMULATIONS

Density functional theory (DFT) calculations were conducted with the software VASP, using the projector augmented wave method [54–57] and the PBE-96 generalized gradient exchange-correlation functional [58].

A. Structure optimization

The lattice constant and the atomic positions were refined to minimize the total energy of the system and the net forces on each ion. A plane-wave energy cutoff of 600 eV was used in all calculations. A $12\times12\times12$ Monkhorst-Pack electronic k mesh was used for the Brillouin-zone integration [59], in the case of FeSi, Fe_3OsSi_4, and Fe_3IrSi_4 unit cells. The optimized unit cells of these structures were used to construct $2\times2\times2$ supercells ($Fe_{32}Si_{32}$, $Fe_{24}Os_8Si_{32}$, and $Fe_{24}Ir_8Si_{32}$) for phonon calculations. These parameters were sufficient for total-energy convergence. In the case of $Fe_{31}OsSi_{32}$ and $Fe_{31}IrSi_{32}$, a $6\times6\times6$ k mesh was used. The primitive unit cell for the FeSi B20 structure contains four formula units. The optimized lattice constant was 4.4492 Å, in good agreement with the reported experimental lattice constants [$a = 4.4747$ Å ($T = 0$ K) and $a = 4.4869$ Å ($T = 300$ K)] [60]. In the case of $Fe_{31}OsSi_{32}$ and $Fe_{31}IrSi_{32}$, the optimized lattice constants are 8.9223 Å ($a = 4.4612$ Å) for $Fe_{31}OsSi_{32}$ and 8.9225 Å ($a = 4.4613$ Å) for $Fe_{31}IrSi_{32}$, which agrees well with experimental value $a = 4.495$ Å at 295 K of $Fe_{0.97}Ir_{0.03}Si$ [15]. The optimized lattice constants for $Fe_{24}Os_8Si_{32}$ are 9.0931 Å ($a = 4.5465$ Å) and 9.09537 Å ($a = 4.5477$ Å) for $Fe_{24}Ir_8Si_{32}$.

B. Lattice dynamics

The phonon dispersions and density of states were computed with the small-displacements method [61], as implemented in the software PHONOPY [62], using 64-atom cells. To describe the doped samples, one Fe atom was substituted with either Os or Ir, corresponding to compositions $Fe_{31}OsSi_{32}$ or $Fe_{31}IrSi_{32}$, for a composition close to $Fe_{0.97}X_{0.03}Si$ ($X =$ Ir, Os). A 6×6×6 Monkhorst-Pack electronic k mesh was used for the Brillouin-zone integration. In the case of FeSi, four atomic displacements were used (two for Fe and two for Si) to calculate the Hellmann-Feynman forces. The replacement of the Fe atom with Os or Ir atoms reduced the symmetry of FeSi $P2_13$ (space group 198) to $R3$ (space group 146) and 128 atomic displacements were used for these supercells. Additional computations were performed on supercells of $Fe_{24}Os_8Si_{32}$ and $Fe_{24}Ir_8Si_{32}$ based on 2×2×2 unit cells of Fe_3IrSi_4 and Fe_3OsSi_4, and 16 atomic displacements were used.

Results along the high-symmetry directions of the primitive cubic reciprocal lattice are shown in Fig. 6. Since the B20 unit cell of FeSi contains eight atoms, there are 24 branches in the phonon dispersions. The optical modes extend up to ∼59 meV due to the Si-Si nearest-neighbor interaction, which is comparable to the highest optic modes in diamond-Si, ∼64 meV [63]. The Si on-site diagonal force constant in FeSi is 12.595 eV/Å^2, close to the corresponding value in diamond-Si (13.445 eV/Å^2) [64]. Our results for phonon-dispersion curves of pure FeSi are in good agreement with previous calculations [65], as well as with our previously reported inelastic neutron-scattering measurements [28].

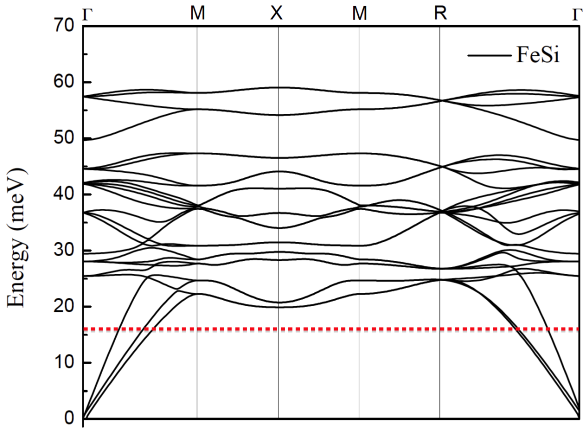

FIG. 6. (Color online) Phonon dispersions of B20 FeSi computed from first principles using density functional theory. The horizontal red-dashed line symbolizes the position of the resonance mode for the Os or Ir impurities in the doped material.

C. Dynamical structure factor

To further compare our first-principles simulations and INS measurements, we computed the dynamical structure factor, using the phonon-dispersion relations and polarization vectors (ϵ_{ds}). We use the following expression [66]:

$$S(\mathbf{Q},E) \propto \sum_s \sum_\tau \frac{1}{E_s} \left| \sum_d \frac{\bar{b}_d}{\sqrt{M_d}} e^{(-W_d + i\mathbf{Q}\cdot\mathbf{r}_d)} (\mathbf{Q}\cdot\epsilon_{ds}) \right|^2 \times \langle n_s + 1 \rangle \delta(E - E_s) \delta(\mathbf{Q} - \mathbf{q} - \tau), \quad (1)$$

where s, τ, and d denote the branch index, reciprocal lattice vector, and atom index in the unit cell, respectively. W_d is the Debye-Waller factor, and $\bar{b}_d$ and M_d are the coherent neutron-scattering length and atomic mass, respectively, for atom d. The Debye-Waller factor is obtained as [66]

$$W_d = \frac{\hbar^2}{4M_d} \sum_s \frac{|\mathbf{Q}\cdot\epsilon_{ds}|^2}{E_s} \times \langle 2n_s + 1 \rangle. \quad (2)$$

In all of the expressions, the wave-vector transfer $\mathbf{Q}$ is related to the phonon wave vector $\mathbf{q}$ through the reciprocal lattice vector of the appropriate Brillouin zone τ as $\mathbf{Q} = \mathbf{q} + \tau$. The result was convoluted with a model for the four-dimensional resolution function of ARCS, as a product of two Gaussians in $\mathbf{Q}$ and E, $R_{\mathbf{Q}_0,E_0}(\mathbf{Q},E) = G_{\sigma_{Q_0}}(\mathbf{Q}_0) \times G_{\sigma_{E_0}(E)}(E)$. The Gaussian $\mathbf{Q}$ resolution used a constant width σ_{Q_0}, while the E-dependent energy resolution $\sigma_{E_0}(E)$ was obtained from an Ikeda-Carpenter model with the instrument parameters for $E_i = 40$ meV and appropriate chopper frequencies. The $S(\mathbf{Q},E)$ intensities were computed on the three-dimensional reciprocal-space $\mathbf{Q}$ grid, and summed over the same integration of $\mathbf{Q}$ ranges used in analyzing the experimental data.

The measured and computed $S(\mathbf{Q},E)$ at 300 K for $\mathbf{Q}$ along $[-3, -3, L]$ are shown in Fig. 7. As can be seen, the agreement between the simulation and experiment is very good [the computed $S(\mathbf{Q},E)$ is scaled by an overall factor as the experimental data were not normalized to absolute units]. The phonon energies are in close agreement, with the calculated energies slightly higher than measured, in part because of the theoretical lattice parameter being 0.8% smaller than the experimental value at 300 K. The relative intensities of the various branches are also in good agreement, and enable the identification of branches based on the polarization conditions. The longitudinal acoustic branches appear only weakly, but remain discernible, along this predominantly transverse path, mainly because of the finite $\mathbf{Q}$-integration volume. Importantly, this indicates that the computed phonon polarization vectors of the various branches are accurate.

D. Density of states

Figure 8(a) shows the calculated total phonon DOS for FeSi, $Fe_{31}OsSi_{32}$, and $Fe_{31}IrSi_{32}$. Comparison with the experimental measurements in Fig. 2 shows very good agreement of the energy range of the spectrum, as well as the position and shape of the features. The experimental spectra are broader largely because of the experimental resolution of

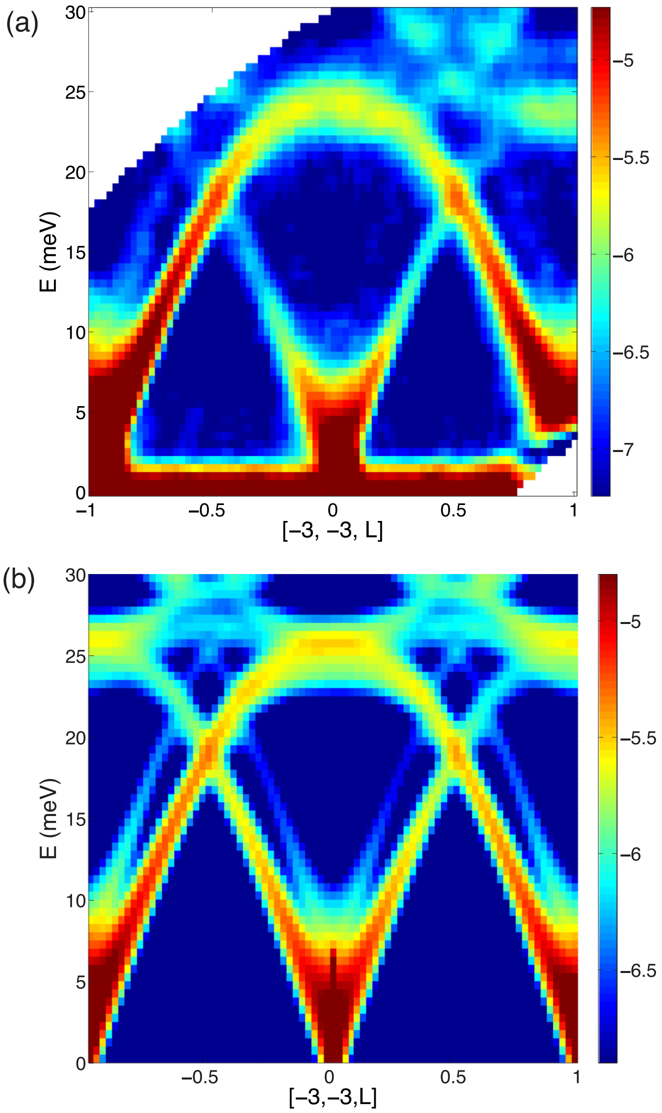

FIG. 7. (Color online) Dynamical structure factor, $S(\mathbf{Q},E)$, of FeSi for $\mathbf{Q}$ along $[-3,-3,L]$ $(-1 \leqslant L \leqslant 1)$. (a) Experimental data measured with ARCS at 300 K. (b) First-principles calculation, with phonon thermal occupation factor set to $T = 300$ K. Integration ranges are $[-3.1,-2.9]$ along $[H,H,0]$ and $[-0.1,0.1]$ along $[K,-K,0]$, for both experimental and simulated data. Note that the strong horizontal bar of intensity for $E < 1.5$ meV in (a) corresponds to experimental background.

the ARCS spectrometer. In addition, the INS generalized phonon DOS is skewed to lower energies, owing to the larger cross section of Fe atoms. This effect was investigated quantitatively in [30] by measuring the Fe-specific partial phonon DOS with nuclear-resonant inelastic x-ray scattering (it does not affect the present discussion). The first-principles calculations for doped samples show excellent agreement with the experimental data. In particular, both Ir and Os impurities lead to an enhancement in spectral weight in the range $12 \leqslant E \leqslant 20$ meV, corresponding to the resonance mode of the heavy impurities and in remarkable agreement with the INS data. The dynamics of the host FeSi are also affected with an overall softening of the spectrum, as well as the formation of a small localized mode above the cutoff of the undoped FeSi, around 62 meV. In addition, Ir doping leads to a larger softening of the spectrum, compared to Os-doped and undoped FeSi.

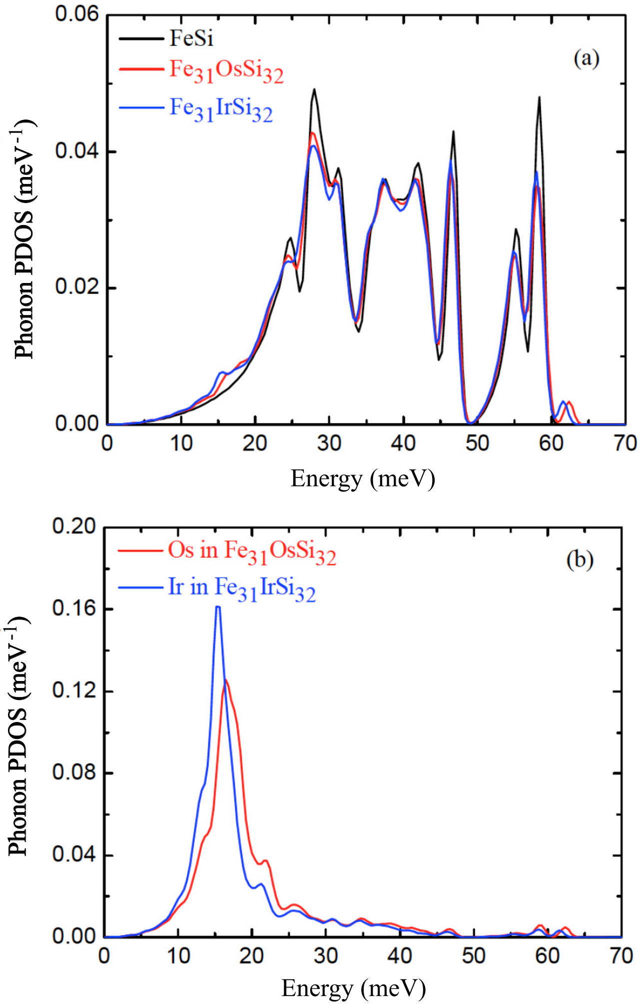

FIG. 8. (Color online) (a) Total phonon density of states for FeSi, $Fe_{31}OsSi_{32}$, and $Fe_{31}IrSi_{32}$. (b) Partial phonon density of states for Ir and Os impurities in $Fe_{31}OsSi_{32}$ and $Fe_{31}IrSi_{32}$. All first-principles calculations were performed at the theoretical equilibrium lattice parameters $a = 4.4492$, 4.4612, and 4.4613 Å, respectively, for FeSi, $Fe_{31}OsSi_{32}$, and $Fe_{31}IrSi_{32}$. All spectra are normalized to unity.

Figure 8(b) shows the normalized partial phonon density of states (PDOS) for Os in $Fe_{31}OsSi_{32}$ and Ir in and $Fe_{31}IrSi_{32}$. In both cases, the partial phonon DOS of impurities is sharply peaked around 17 meV, with little spectral weight above 23 meV. As can be seen, the vibration spectra of these heavy impurities are nearly completely decoupled from the host spectrum, corresponding to a resonance behavior. According to these calculated spectra, the average phonon energies are 20.4 and 18.6 meV for Os and Ir impurities, respectively, compared with 32.5 meV for the Fe atoms in pure FeSi (and 37.1 meV for the average FeSi host). Figure 11 compares the PDOS of the Os atom in $Fe_{31}OsSi_{32}$ and $Fe_{24}Os_8Si_{32}$, and the PDOS of Ir in $Fe_{31}IrSi_{32}$ and $Fe_{24}Ir_8Si_{32}$. The similarity in the impurity spectra for these different cells indicates that the interaction

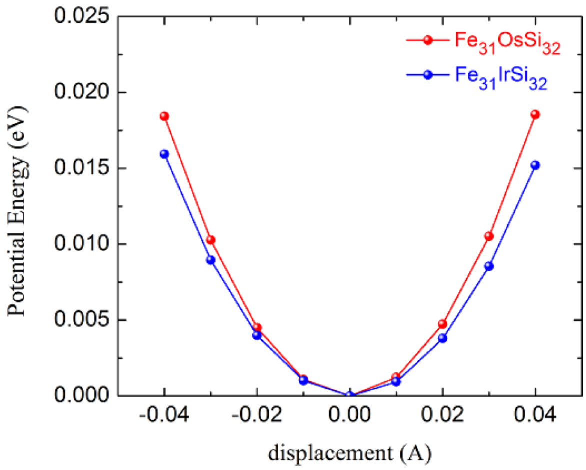

FIG. 9. (Color online) Local potential-energy curves for Os and Ir impurities in FeSi. The calculations were performed on 64-atom cells of $Fe_{31}OsSi_{32}$ and $Fe_{31}IrSi_{32}$, with the impurity displaced along [100].

between impurity and host are relatively short ranged. We also show below that the position of the resonance mode can be well reproduced with a local impurity model based on a Green's-function approach, neglecting all impurity-impurity interactions.

The softening upon Ir doping shown in Figs. 8(a) and 8(b) can be attributed to the screening by the extra carriers. Figure 9 shows the potential energy as a function of impurity displacement along [100]. As can be seen, the potential curve is softer for $Fe_{31}IrSi_{32}$ than for $Fe_{31}OsSi_{32}$. The corresponding on-site force constant for the Ir impurity is $19.46\ \text{eV}/\text{Å}^2$, 18% smaller than for the Os impurity ($23.08\ \text{eV}/\text{Å}^2$), while both are larger than the Fe on-site force constant in pure FeSi ($15.58\ \text{eV}/\text{Å}^2$). Transport measurements in Fig. 1(a) show that small amounts of substitutional Ir dopants lead to a metallic resistivity. The metallic character of $Fe_{31}IrSi_{32}$ is also seen in the electronic density of states computed from first principles, shown in Fig. 10, whereas FeSi and $Fe_{31}OsSi_{32}$ are narrow-gap semiconductors. In a similar fashion, doping with Al on the Si site leads to a metallic state and softer phonons [30]. A similar effect was observed in the T dependence of phonons in FeSi, with $T \gtrsim 300$ K leading to metallization with a pronounced concomitant phonon softening [24,25,28].

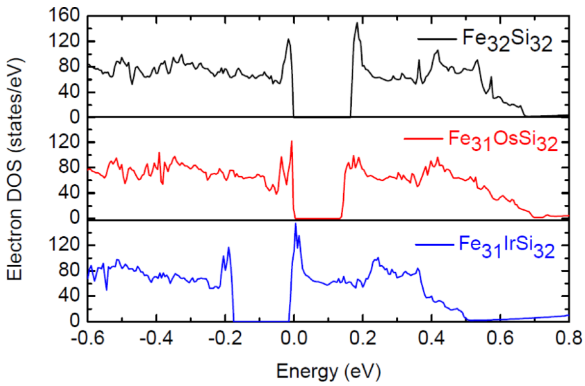

FIG. 10. (Color online) Electronic DOS, $N(E)$, for FeSi, $Fe_{31}OsSi_{32}$, and $Fe_{31}IrSi_{32}$, computed on the relaxed cells. The Fermi level is taken as the origin of energy (at the top of the valence band in the case of FeSi and $Fe_{31}OsSi_{32}$).

E. Green's-functions modeling

The partial densities of states for Os and Ir were also calculated using the Green's-function approach of Mannheim [67–69]. This analytical model for the impurity partial DOS is based on a simplified local perturbation of force constants and assumes dilute impurities (no impurity-impurity interactions). With these approximations, the impurity partial DOS, $g'(\omega)$, depends on the phonon DOS of the host crystal, $g(\omega)$, and only two additional parameters: the mass ratio between host and impurity atoms M/M', and the ratio in first-nearest-neighbor force constants, Φ/Φ'. The impurity spectrum is then obtained as [69]

$$g'(\omega) = \frac{M}{M'} g(\omega)\left\{[1+\rho(\omega)\,S(\omega)]^2 + \left[\frac{\pi}{2}\omega g(\omega)\rho(\omega)\right]^2\right\}^{-1}, \tag{3}$$

where

$$\rho(\omega) = \frac{M}{M'} - 1 + \omega^2[1-(\Phi/\Phi')]/\mu(2), \tag{4}$$

$$S(\omega) = \mathcal{P}\int_0^\infty \omega'^2(\omega'^2-\omega^2)^{-1} g(\omega')d\omega', \tag{5}$$

$$\mu(n) = \int_0^\infty \omega^n\, g(\omega)d\omega, \tag{6}$$

with $\mathcal{P}$ denoting the Cauchy principal value, and where we have discarded any localized mode above the phonon cutoff. We evaluate these equations with the ratio of on-site DFT force constants above, dismissing complications of the sevenfold coordination shell. The host phonon DOS $g(\omega)$ was taken from the DFT result of Fig. 8(a). Results are shown in Fig. 11(c). We note that this simple impurity model matches the results from the supercell DFT calculations surprisingly well. Both approaches lead to a clear resonance mode centered between 15 and 19 meV, with a Lorentzian-like shape. It can be noticed that the Green's-function model predicts a slightly larger impurity resonance frequency than the DFT calculation. This is in part because impurities lead to a local relaxation of atomic positions and an overall expansion of the cell, which are taken into account in the DFT calculations (relaxed volume and ionic positions), but not in the Green's-function model.

Further, the knowledge of the vibration spectrum of the impurity, $g'(\omega)$, enables us to compute the dynamical structure factor $S(\mathbf{Q},E)$ of the crystal with impurity, from the local perturbation to the lattice Green's function. The dynamical structure contribution from phonon branch σ is $S_{\sigma,\text{coh}} \propto \text{Im}\mathcal{G}_\sigma$, where the perturbed lattice Green's function $\mathcal{G}$ can be expressed in terms of the self-energy Σ as

$$\mathcal{G}_\sigma(\mathbf{q},\omega) \propto \frac{1}{m\left[\omega^2-\omega_0^2(\mathbf{q},\sigma)\right] - c\,\Sigma_\sigma(\mathbf{q},\omega)}, \tag{7}$$

with $\omega_0(\mathbf{q},\sigma)$ the unperturbed dispersion frequency of branch σ. The self-energy of phonons in branch σ owing to the

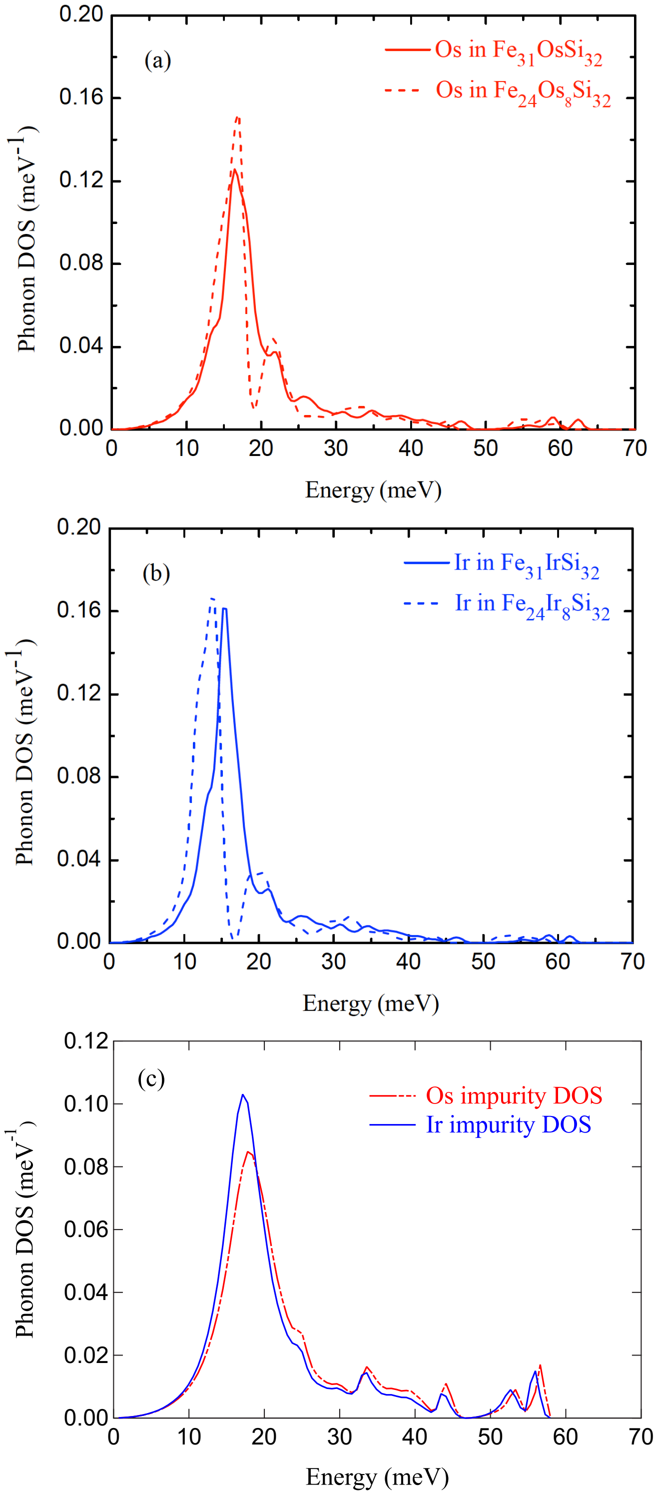

FIG. 11. (Color online) Partial phonon DOS of (a) Os and (b) Ir atoms computed from first principles for the supercells $Fe_{31}XSi_{32}$ (solid curves) and $Fe_{24}X_8Si_{32}$ (dashed curves), with $X =$ Os, Ir. (c) The isolated-impurity partial DOS for Os and Ir derived from the simplified Green's-function model described in the text.

interaction with the impurity resonance mode is modeled as

$$\Sigma_\sigma(\mathbf{q},\omega) \approx \frac{V^2}{m\left[\omega^2 - \omega_R^2 - i\,2\omega_R\gamma\right]}, \qquad (8)$$

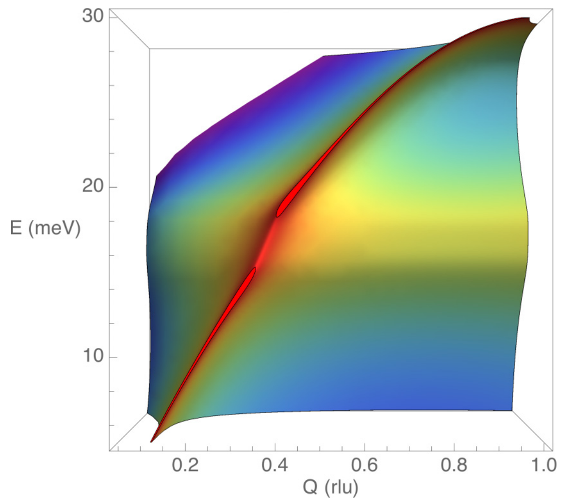

FIG. 12. (Color online) Dynamical structure factor, $S(\mathbf{Q},E)$, computed using the Green's-function model described in the text, for an impurity resonance mode of energy $E_R = 17$ meV and a sine-wave acoustic dispersion branch.

with γ the damping of the impurity resonance mode centered at ω_R, which was extracted by fitting the impurity vibrational spectrum of Fig. 11(c), $g'(\omega)$, with a Lorentzian $\mathcal{L}_{\omega_R,\gamma}(\omega)$. For the Os (Ir) impurity, we obtain $\omega_R = 18.7$ meV and $\gamma = 7.9$ meV ($\omega_R = 17.1$ meV and $\gamma = 5.7$ meV). The interaction strength V was taken as an adjustable parameter. The resulting $\mathrm{Im}\mathcal{G}_\sigma(\mathbf{q},\omega)$ obtained with this approach, for a simplified (sinusoidal) transverse acoustic dispersion branch, is shown in Fig. 12. As can be seen, a clear kink develops in the acoustic dispersions as it crosses the impurity resonance mode, accompanied by a suppression in the spectral intensity (magnitude of S). This behavior is in very good agreement with the INS measurement of $S(\mathbf{Q},\omega)$ in Figs. 3 and 4, validating the interpretation of the kink in the dispersions in terms of the interaction with the impurity resonance mode. A more quantitative modeling of this effect, based on numerical simulations of configuration-averaged supercells to describe the alloy, is presented in the next section.

F. Disorder-induced lifetimes

We investigated from first principles the disorder-induced lifetimes by simulating many large supercells, in which the Os impurities are randomly distributed. To handle the computational expense associated with large supercells, we employ a recently developed method [70]. The disorder-induced phonon lifetimes are encoded in the configurationally averaged spectral function $\langle A_n(\mathbf{q},E)\rangle = \sum_c A_n^c(\mathbf{q},E)$, where $A_n^c(\mathbf{q},E)$ is the spectral function of configuration c at momentum $\mathbf{q}$ and energy E, projected onto atom type n. The latter is obtained by using the supercell eigenvalues and eigenvectors of configuration c in the unfolding formula of Ref. [71]. The spectral function for $Fe_{0.96}Os_{0.04}Si$ was obtained from 10 supercells with 320 atoms on average. The results are shown in Fig. 13. The colors correspond to the three atom types, i.e.,

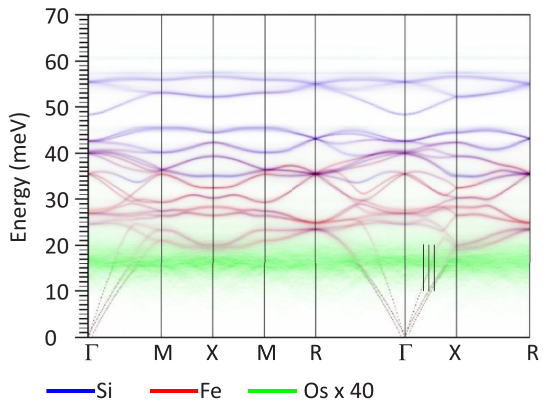

FIG. 13. (Color online) Atomically resolved configuration-averaged phonon spectral function $\langle A_n(\mathbf{q},E)\rangle$ of $\mathrm{Fe_{0.96}Os_{0.04}Si}$ obtained from first-principles calculations of 10 supercells with 320 atoms on average. The vertical lines correspond to fixed momenta curves in Fig. 14.

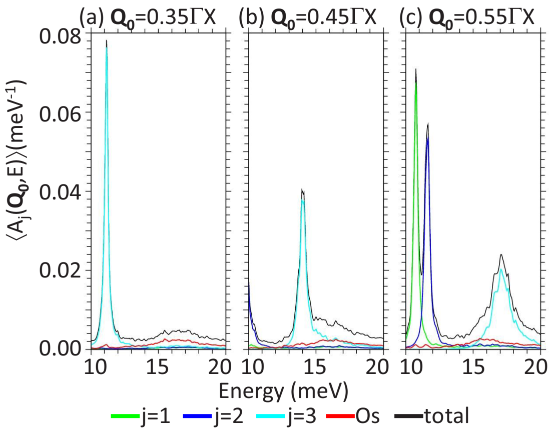

FIG. 14. (Color online) Band-resolved configuration-averaged phonon spectral function $\langle A_j(\mathbf{q}_0,E)\rangle$ of $\mathrm{Fe_{0.96}Os_{0.04}Si}$ at (a) $\mathbf{q}_0 = 0.35\Gamma X$, (b) $\mathbf{q}_0 = 0.45\Gamma X$, and (c) $\mathbf{q}_0 = 0.55\Gamma X$, corresponding to the vertical lines in Fig. 13. Bands $j = 1,2$ correspond to transverse acoustic modes and $j = 3$ to longitudinal acoustic modes.

Si, Fe, and Os, where the intensity corresponding to Os is enhanced by a factor of 40 for better visibility.

As can be seen in Fig. 13, the simulation predicts a clear impurity band corresponding to the Os resonance modes. The band is centered around 17 meV, in good agreement with experiments (Figs. 2 and 5), and also with the results obtained directly from DFT (Figs. 8 and 11). The flatness of the band indicates the incoherent nature of the Os modes. Upon close inspection, similar flat features can be seen around 57 and 61 meV, which are localized modes emerging out of the Si-dominated optical branches. These reflect the strong coupling of the Os impurities with their neighboring Si atoms. Finally, the Os impurities also alter the acoustic branches which carry most of the heat and thus directly control the thermal conductivity. As the acoustic branches approach the energy of the impurity band, they show a kink in their dispersion and a strongly reduced spectral weight, as was noticed from the experimental data (Figs. 3 and 4) and the theoretical Green's-function modeling (Fig. 12).

To further explore the interaction of acoustic branches with the impurity resonance mode, we plot in Fig. 14 the band-resolved configurationally averaged spectral function $\langle A_j(\mathbf{q_0},E)\rangle$ of band index j at the three momenta $\mathbf{q}_0 = 0.35\Gamma X$, $\mathbf{q}_0 = 0.45\Gamma X$, and $\mathbf{q}_0 = 0.55\Gamma X$, corresponding to the vertical lines in Fig. 13. To resolve the bands, we represent the spectral operator in the eigenbasis of the undoped system [79], in this case the phonon eigenvectors for the FeSi host system. Bands $j = 1,2$ correspond to the transverse acoustic modes and $j = 3$ to longitudinal acoustic modes. We note that the two TA branches are slightly offset in energy, which is a result of numerical noise, as these modes are degenerate by symmetry along the direction $\Gamma - X$.

Focusing on the longitudinal-acoustic (LA) branch ($j = 3$) in Fig. 14, one can observe a clear broadening in energy and momentum space, corresponding to the inverse lifetime and mean free path, increasing as it approaches the impurity band. At $\mathbf{q}_0 = 0.35\Gamma X$, in Fig. 14(a), the LA mode shows a small but finite disorder-induced energy broadening, of the order of 1 meV. At $\mathbf{q}_0 = 0.45\Gamma X$, in Fig. 14(b), the LA branch enters the bottom of the impurity band and shows a large asymmetric broadening towards higher energy. At $\mathbf{q}_0 = 0.55\Gamma X$, in Fig. 14(c), the LA branch appears in the middle of the impurity band and shows the largest energy broadening, of the order of 5 meV. Similarly, a broadening in momentum space can also be noted if we focus our attention on a fixed energy. For example, at the fixed energy $E = 17$ meV, the spectral weight of the LA branch $j = 3$ reduces from 19.49 eV^{-1} at $\mathbf{q_0} = 0.55\Gamma X$ [Fig. 14(c)] to 1.97 eV^{-1} at $\mathbf{q}_0 = 0.45\Gamma X$ [Fig. 14(b)] to 0.85 eV^{-1} at $\mathbf{q}_0 = 0.35\Gamma X$ [Fig. 14(a)]. These broadenings are a direct consequence of the hybridization of the acoustic branches with the impurity band. They qualitatively reproduce the spectral weight variations observed in the INS data, and directly show the scattering of phonons by the heavy-impurity resonance mode, which suppresses the thermal conductivity.

We note several important aspects from our findings. From both INS experiments and simulations, we identified a clear resonance mode associated with the vibration of heavy Os and Ir atoms, which are dynamically decoupled from the phonon dispersions of the host lattice. The widely used expressions for mass-mismatch scattering of phonons by point defects are typically derived using perturbation theory [11,12], assuming that the dispersion frequencies in the crystal are unchanged. For large mass contrast, this assumption is expected to break down, since a new resonance mode emerges, and it can hybridize with the acoustic phonon branches as shown here. These results should motivate further theoretical investigations of phonon-scattering processes in the regime of strong mass perturbations.

VI. CONCLUSION

Using inelastic neutron scattering, we have observed the formation of a heavy-impurity resonance mode in FeSi doped with a few percent of Ir or Os. The resonance mode occurs in the range of acoustic phonon dispersions, with an energy $E_R \simeq 17$ meV, with little dispersive character. The resonance mode is rather broad, with a width ∼6 meV. Our first-principles simulations on supercells, Green's-function modeling, and quasiparticle spectral function calculations reproduce our experimental observations remarkably well, in particular showing the resonance mode formation and its hybridization with the acoustic modes. We do not observe a fully developed anticrossing behavior, but the acoustic modes are considerably broadened in the vicinity of the resonance. These observations directly validate the strategy which consists of using heavy dopants to scatter phonons and suppress thermal conductivity in thermoelectrics. However, our results also show that in the regime of strong mass perturbation, some of the approximations used to derive commonly used formulas for mass-defect phonon scattering break down.

ACKNOWLEDGMENTS

Neutron-scattering work by O.D. was supported by the US Department of Energy, Office of Science, Basic Energy Sciences, Materials Sciences and Engineering Division, through the Office of Science Early Career Research Program. A.F.M. and B.C.S. were supported by the US Department of Energy, Office of Science, Basic Energy Sciences, Materials Sciences and Engineering Division. J.M. and C.W.L. were supported by the US Department of Energy, Office of Basic Energy Sciences, as part of the S3TEC Energy Frontier Research Center, DOE Grant No. DE-SC0001299. I.I.A. was sponsored by the Laboratory Directed Research and Development Program of ORNL. T.B. was supported as a Wigner Fellow at the Oak Ridge National Laboratory. The phonon modeling work was performed within the Center for Accelerating Materials Modeling of SNS data, supported by the US Department of Energy, Basic Energy Sciences, Materials Sciences and Engineering Division (J.L.N., O.D.). The research at Oak Ridge National Laboratory's Spallation Neutron Source and High Flux Isotope Reactor was sponsored by the Scientific User Facilities Division, Office of Basic Energy Sciences, US Department of Energy. This research used resources of the National Energy Research Scientific Computing Center, a DOE Office of Science User Facility supported by the Office of Science of the US Department of Energy under Contract No. DE-AC02-05CH11231.

[1] G. J. Snyder and E. S. Toberer, Nat. Mater. **7**, 105 (2008).
[2] A. Béraud, J. Kulda, I. Yonenaga, M. Foret, B. Salce, and E. Courtens, Physica B **350**, 254 (2004).
[3] Jivtesh Garg, Nicola Bonini, Boris Kozinsky, and Nicola Marzari, Phys. Rev. Lett. **106**, 045901 (2011).
[4] D. P. Young, P. Khalifah, and R. J. Cava, J. Appl. Phys. **87**, 317 (2000).
[5] P. Maji, N. J. Takas, D. K. Misra, H. Gabrisch, K. Stokes, and P. F. P. Poudeu, J. Solid State Chem. **183**, 1120 (2010).
[6] Xiao Yan, Weishu Liu, Hui Wang, Shuo Chen, Junichiro Shiomi, Keivan Esfarjani, Hengzhi Wang, Dezhi Wang, Gang Chen, and Zhifeng Ren, Energy Environ. Sci. **5**, 7543 (2012).
[7] Hanhui Xie, Heng Wang, Chenguang Fu, Yintu Liu, G. Jeffrey Snyder, Xinbing Zhao, and Tiejun Zhu, Sci. Rep. **4**, 6888 (2014).
[8] V. Keppens, D. Mandrus, B. C. Sales, B. C. Chakoumakos, P. Dai, R. Coldea, M. B. Maple, D. A. Gajewski, E. J. Freeman, and S. Bennington, Nature (London) **395**, 876 (1998).
[9] M. M. Koza, M. R. Johnson, R. Viennois, H. Mutka, L. Girard, and D. Ravot, Nat. Mater. **7**, 805 (2008).
[10] Mona Zebarjadi, Keivan Esfarjani, Jian Yang, Z. F. Ren, and Gang Chen, Phys. Rev. B **82**, 195207 (2010).
[11] P. G. Klemens, in *Solid State Physics, Advances in Research and Applications*, edited by F. Seitz and D. Turnbull (Academic Press, New York, 1958), Vol. 7, pp. 1–98.
[12] S. I. Tamura, Phys. Rev. B **27**, 858 (1983).
[13] L. Pauling and A. M. Soldate, Acta Crystallogr. **1**, 212 (1948).
[14] D. P. Dobson, L. Vocadlo, and I. G. Wood, Am. Mineral. **87**, 784 (2002).
[15] B. C. Sales, E. C. Jones, B. C. Chakoumakos, J. A. Fernandez-Baca, H. E. Harmon, J. W. Sharp, and E. H. Volckmann, Phys. Rev. B **50**, 8207 (1994).
[16] D. Mandrus, J. L. Sarrao, A. Migliori, J. D. Thompson, and Z. Fisk, Phys. Rev. B **51**, 4763 (1995).
[17] R. P. Krentsis, G. I. Kalishevich, P. V. Geld, and L. P. Andreeva, Izv. Vyssh. Vchebon. Zaved. Fiz. **1**, 153 (1972) [Sov. Phys. **15**, 193 (1972)].
[18] V. I. Anisimov, S. Y. Ezhov, I. S. Elfimov, I. V. Solovyev, and T. M. Rice, Phys. Rev. Lett. **76**, 1735 (1996).
[19] J. F. DiTusa, K. Friemelt, E. Bucher, G. Aeppli, and A. P. Ramirez, Phys. Rev. Lett. **78**, 2831 (1997).
[20] J. F. DiTusa, K. Friemelt, E. Bucher, G. Aeppli, and A. P. Ramirez, Phys. Rev. B **58**, 10288 (1998).
[21] V. Jaccarino, G. K. Wertheim, J. H. Wernick, L. R. Walker, and Sigurds Arajs, Phys. Rev. **160**, 476 (1967).
[22] L. F. Mattheiss and D. R. Hamann, Phys. Rev. B **47**, 13114 (1993).
[23] C. Fu, M. P. C. M. Krijn, and S. Doniach, Phys. Rev. B **49**, 2219 (1994).
[24] T. Jarlborg, Phys. Lett. A **236**, 143 (1997).
[25] T. Jarlborg, Phys. Rev. B **59**, 15002 (1999).
[26] T. Jarlborg, J. Magn. Magn. Mater. **283**, 238 (2004).
[27] T. Jarlborg, Phys. Rev. B **76**, 205105 (2007).
[28] O. Delaire, K. Marty, M. B. Stone, P. R. C. Kent, M. S. Lucas, D. L. Abernathy, D. Mandrus, and B. C. Sales, Proc. Natl. Acad. Sci. USA **108**, 4725 (2011).
[29] B. C. Sales, O. Delaire, M. A. McGuire, and A. F. May, Phys. Rev. B **83**, 125209 (2011).
[30] O. Delaire, I. I. Al-Qasir, J. Ma, A. M. dos Santos, B. C. Sales, L. Mauger, M. B. Stone, D. L. Abernathy, Y. Xiao, and M. Somayazulu, Phys. Rev. B **87**, 184304 (2013).
[31] K. Ishizaka, T. Kiss, T. Shimojima, T. Yokoya, T. Togashi, S. Watanabe, C. Q. Zhang, C. T. Chen, Y. Onose, Y. Tokura, and S. Shin, Phys. Rev. B **72**, 233202 (2005).
[32] M. Arita *et al.*, Phys. Rev. B **77**, 205117 (2008).
[33] D. Menzel, P. Popovich, N. N. Kovaleva, J. Schoenes, K. Doll, and A. V. Boris, Phys. Rev. B **79**, 165111 (2009).
[34] J. Kunes and V. I. Anisimov, Phys. Rev. B **78**, 033109 (2008).

[35] J. M. Tomczak, K. Haule, and G. Kotliar, Proc. Natl. Acad. Sci. USA **109**, 3243 (2012).
[36] D. Zur, D. Menzel, I. Jursic, J. Schoenes, L. Patthey, M. Neef, K. Doll, and G. Zwicknagl, Phys. Rev. B **75**, 165103 (2007).
[37] M. Klein, D. Zur, D. Menzel, J. Schoenes, K. Doll, J. Röder, and F. Reinert, Phys. Rev. Lett. **101**, 046406 (2008).
[38] N. Manyala, J. F. DiTusa, G. Aeppli, and A. P. Ramirez, Nature (London) **454**, 976 (2008).
[39] L. Degiorgi, M. B. Hunt, H. R. Ott, M. Dressel, B. J. Feenstra, G. Grner, Z. Fisk, and P. Canfield, Europhys. Lett. **28**, 341 (1994).
[40] E. Knittle and Q. Williams, Geophys. Res. Lett. **22**, 445 (1995).
[41] J. F. Lin, A. J. Campbell, D. L. Heinz, and Guoyin Shen, J. Geophys. Res. **108**, 2045 (2003).
[42] R. Caracas and R. Wentzcovitch, Geophys. Res. Lett. **31**, L20603 (2004).
[43] A. Damascelli, K. Schulte, D. van der Marel, and A. A. Menovsky, Phys. Rev. B **55**, R4863 (1997).
[44] A.-M. Racu, D. Menzel, J. Schoenes, and K. Doll, Phys. Rev. B **76**, 115103 (2007).
[45] O. Delaire, M. S. Lucas, J. A. Muñoz, M. Kresch, and B. Fultz, Phys. Rev. Lett. **101**, 105504 (2008).
[46] O. Delaire, M. Kresch, J. A. Muñoz, M. S. Lucas, J. Y. Y. Lin, and B. Fultz, Phys. Rev. B **77**, 214112 (2008).
[47] O. Delaire, A. F. May, M. A. McGuire, W. D. Porter, M. S. Lucas, M. B. Stone, D. L. Abernathy, V. A. Ravi, S. A. Firdosy, and G. J. Snyder, Phys. Rev. B **80**, 184302 (2009).
[48] D. L. Abernathy, M. B. Stone, M. J. Loguillo, M. S. Lucas, O. Delaire, X. Tang, J. Y. Y. Lin, and B. Fultz, Rev. Sci. Instrum. **83**, 015114 (2012).
[49] http://www.mantidproject.org (unpublished).
[50] O. Delaire and C. Stassis, in *Phonon Studies in Characterization of Materials* (Wiley, New York, 2012), pp. 1–22.
[51] P. H. Dederichs, K. Schroeder, and R. Zeller, *Point Defects in Metals II: Dynamical Properties and Diffusion Controlled Reactions* (Springer, Berlin, 1980).
[52] O. Delaire, T. Swan-Wood, and B. Fultz, Phys. Rev. Lett. **93**, 185704 (2004).
[53] L. Pintschovius, D. Reznik, F. Weber, P. Bourges, D. Parshall, R. Mittal, S. L. Chaplot, R. Heid, T. Wolf, D. Lamago, and J. W. Lynn, Appl. Cryst. **47**, 1472 (2014).
[54] G. Kresse and J. Furthmüller, Comput. Mater. Sci. **6**, 15 (1996).
[55] G. Kresse and J. Furthmüller, Phys. Rev. B **54**, 11169 (1996).
[56] P. E. Blöchl, Phys. Rev. B **50**, 17953 (1994).
[57] G. Kresse and D. Joubert, Phys. Rev. B **59**, 1758 (1999).
[58] J. P. Perdew, K. Burke, and M. Ernzerhof, Phys. Rev. Lett. **77**, 3865 (1996).
[59] H. J. Monckhorst and J. D. Pack, Phys. Rev. B **13**, 5188 (1976).
[60] L. Vočadlo, K. S. Knight, G. D. Price, and I. G. Wood, Phys. Chem. Miner. **29**, 132 (2002).
[61] K. Parlinski, Z.-Q. Li, and Y. Kawazoe, Phys. Rev. Lett. **78**, 4063 (1997).
[62] Atsushi Togo, Fumiyasu Oba, and Isao Tanaka, Phys. Rev. B **78**, 134106 (2008). PHONOPY software: http://phonopy.sourceforge.net/ (unpublished).
[63] M. T. Yin and M. L. Cohen, Phys. Rev. B **25**, 4317 (1982).
[64] M. Aouissi, I. Hamdi, N. Meskini, and A. Qteish, Phys. Rev. B **74**, 054302 (2006).
[65] Y. N. Zhao, H. L. Han, Y. Yu, W. H. Xue, and T. Gao, Europhys. Lett. **85**, 47005 (2009).
[66] G. L. Squires, *Introduction to the Theory of Thermal Neutron Scattering* (Cambridge University Press, Cambridge, 1978).
[67] P. D. Mannheim, Phys. Rev. **165**, 1011 (1968).
[68] P. D. Mannheim and S. S. Cohen, Phys. Rev. B **4**, 3748 (1971).
[69] M. Seto, Y. Kobayashi, S. Kitao, R. Haruki, T. Mitsui, Y. Yoda, S. Nasu, and S. Kikuta, Phys. Rev. B **61**, 11420 (2000).
[70] This is a different method, to be published, which is based on the same principles as the method presented in Ref. [78], except that it applies to force-constant matrices of phonons rather than Wannier function based tight-binding Hamiltonians of electrons.
[71] W. Ku, T. Berlijn, and C.-C. Lee, Phys. Rev. Lett. **104**, 216401 (2010). For the other unfolding methods, see [72–77].
[72] S. Baroni, S. de Gironcoli, and P. Giannozzi, Phys. Rev. Lett. **65**, 84 (1990).
[73] T. B. Boykin and G. Klimeck, Phys. Rev. B **71**, 115215 (2005).
[74] F. Giustino, Jonathan R. Yates, I. Souza, M. L. Cohen, and S. G. Louie, Phys. Rev. Lett. **98**, 047005 (2007).
[75] V. Popescu and A. Zunger, Phys. Rev. Lett. **104**, 236403 (2010).
[76] M. W. Haverkort I. S. Efimov, and G. A. Sawatzky, arXiv:1109.4036.
[77] P. B. Allen, T. Berlijn, D. A. Casavant, and J. M. Soler, Phys. Rev. B **87**, 085322 (2013).
[78] T. Berlijn, D. Volja, and W. Ku, Phys. Rev. Lett. **106**, 077005 (2011).
[79] T. Berlijn, C.-H. Lin, W. Garber, and W. Ku, Phys. Rev. Lett. **108**, 207003 (2012).